

Synthesis of RGO–Co doped ZnO/PANI hybrid composite for supercapacitor application

R. Karthik¹ · S. Thambidurai¹

Received: 17 October 2016 / Accepted: 13 March 2017 / Published online: 23 March 2017
© Springer Science+Business Media New York 2017

Abstract In this paper, reduced graphene oxide–cobalt doped ZnO/polyaniline (RGO–CZO/PANI) hybrid composites were synthesized through the two step approach: Cobalt doped ZnO particles on RGO sheets by a simple chemical co-precipitation method, followed by coating with PANI through in situ polymerization method. Morphological and structural properties were characterized by X-ray diffraction, Fourier transform infrared spectroscopy, Ultraviolet–Visible absorption spectra, scanning electron microscopy and transmission electron microscopy. Electrochemical performance of the RGO–CZO/PANI hybrid composites were carried out by cyclic voltammetry, galvanostatic charge–discharge and electrochemical impedance spectroscopy in 1M H₂SO₄ electrolyte medium. The findings show that the charge storage of RGO–CZO/PANI hybrid composite is mainly due to the pseudocapacitance (reversible redox reaction) behavior. The highest specific capacitance of 515 F g⁻¹ with the energy density of 370 Wh kg⁻¹ and power density of 3.1 kW kg⁻¹ could be achieved (For three electrode system) in the potential region between –0.2 and 1.0. Notably, in a two-electrode system, the specific capacitance, energy density and power density of the RGO–CZO/PANI symmetric supercapacitor was obtained to be 208 F g⁻¹, 28.88 Wh kg⁻¹ and 0.694 kW kg⁻¹, respectively. The results manifest that the synthesized RGO–CZO/PANI hybrid composite is the promising electrode material for supercapacitor applications.

1 Introduction

Owing to the increase in energy consumption in modern society, the development of renewable and sustainable energy source is urgently needed. The growing demand for portable energy and power system electric vehicles are an essential in short period. The energy conversion and storage device have attracted much attention due to the deteriorating environmental pollution and depletion of fossil fuel [1]. Vast work has been done in the improvement of super capacitor materials when compared to rechargeable batteries because they provide high energy and power density with low maintenance cost. Super capacitor can be classified into two categories such as electric double layer and faradic pseudocapacitor. (i) For the electric double layer capacitor (EDL); the charge is stored on the electrode surface due to the adsorption desorption phenomenon, normally activated carbons are used in the EDL. In other words inert and high conductive carbon materials that store and release energy by charge separation at the electrochemical interface between an electrode and electrolyte (ii) Faradic pseudocapacitor; the charge is stored through the surface redox reactions based on electroactive material such as transition metal oxides and conducting polymers [1]. The important achievements of modern electrochemistry are the development of electron-conducting polymers such as polyaniline (PANI), polythiophene and polypyrrole are used in supercapacitors. Among the conducting polymers, polyaniline is one of the most extensively used conducting materials. It has good electrical conductivity and environmental stability. The carbon backbone of the polymer matrix contained some positively charged nitrogen atom which is regulating the charges and keeping the charge neutrality of the composite material [2]. However, the main drawback of PANI is poor mechanical and electrical stability during

✉ S. Thambidurai
sthambi01@yahoo.co.in

¹ Department of Industrial Chemistry, School of Chemical Sciences, Alagappa University, Karaikudi, Tamil Nadu 630 003, India

the charge/discharge process. Hybrid composite material is considered as a true electrode material for super capacitor.

As is well known, reduced graphene oxide (RGO) has triggered an exciting new area in the field of carbon nano science by always increasing scientific and technological impetus [3, 4]. It contained less amount of oxygen functional group such as hydroxyl, epoxide and carboxyl moieties. These oxygen functional moieties can act as nucleation centers or anchoring sites for the attachment of metal oxides particles and polymer matrixes. Furthermore, it plays a dynamic role that not only restricts the agglomeration of metal oxide particles, but also enhances the chemical and physical properties of the hybrid composite material. It is used as the supporting platform for the attachment of metal oxides to produce the hybrid composite for catalytic and capacitive behavior applications [5].

Further, the effect of pseudocapacitance for improving the total capacitance of carbon material combined conducting polymer hybrid materials by quick Faradaic reactions have been realized by insertion of electro active transition metal oxides such as ZnO, Co_2O_3 , RuO_2 , MnO_2 , TiO_2 and Fe_2O_3 etc. [6]. Co_2O_3 and ZnO are the well-known transition metal oxides. ZnO is not important only due to its electronic, optical, electrochemical and electro catalytic properties, but also for thermo-electric properties as well [7, 8]. The Co_2O_3 -based composites have demonstrated great potentials in the fields of supercapacitor, heterogeneous catalyst, electrochemical sensors and Li-ion batteries [9–13]. However, ZnO usually delivers poor rate capability and reversibility during the charge/discharge process due to its large crystalline size. Therefore, to modify the crystal size of ZnO and increase the electrical conductivity of the whole electrode is highly desired. Much more efforts have been expended to modify the crystal size by doping mechanism and increase the electrical conductivity by incorporating them into carbonaceous material and conducting polymers such as graphene and polyaniline.

In recent years, many researchers are interested in the synthesis of different composites using RGO, metal oxides and polyaniline based materials such as RGO–ZnO, [14] graphene– Co_2O_3 [15] Co–ZnO, [16] sulfur-polyaniline-graphene composite, [17] RGO– Co_2O_3 , [18] PANI– Co_2O_3 , [19] graphene– SnO_2 –PANI, [20] RGO– Fe_2O_3 –PANI [21] and PANI– TiO_2 –graphene oxide [22]. In this context, the ternary composites composed of carbon based materials, conducting conjugated polymers and transition metal oxides have been explored and demonstrated improvement in the electrochemical behavior which delivers a new direction for the fabrication of the next generation high performance supercapacitor. However, all the literature reports focus on the single metal oxide inserted between the conducting polymer and carbon based material. To the best of our knowledge, reduced graphene oxide-cobalt doped ZnO/

polyaniline hybrid composite for supercapacitor application has not been reported yet.

In the present paper, the RGO–CZO/PANI hybrid composites were synthesized by a two-step route. The Co doped ZnO was successfully seated on the RGO sheet by a simple chemical co-precipitation method, then an aniline monomer was polymerized and interact with Co doped ZnO/RGO in a molecular level. The morphology and structural features of the synthesized composites were studied by FTIR, XRD, Ultraviolet–Visible (UV–Vis), scanning electron microscopy (SEM) and transmission electron microscopy (TEM) analysis. The supercapacitive characteristics were evaluated by cyclic voltammetry (CV), galvanostatic charge–discharge (GCD) and electrochemical impedance spectroscopy (EIS) with 1M H_2SO_4 as the electrolyte.

2 Experimental

2.1 Materials

Graphite powder was purchased from loba chemie Pvt. Ltd., Mumbai, India. Zinc nitrate ($\text{Zn}(\text{NO}_3)_2 \cdot 6\text{H}_2\text{O}$), cobalt nitrate ($\text{Co}(\text{NO}_3)_2 \cdot 6\text{H}_2\text{O}$), hydrogen peroxide (H_2O_2), sodium nitrate (NaNO_3), potassium permanganate (KMnO_4), sulfuric acid (H_2SO_4), hydrochloric acid (HCl), sodium hydroxide (NaOH), hydrazine hydrate, aniline ($\text{C}_6\text{H}_5\text{NH}_2$), ammonium peroxydisulfate ($(\text{NH}_4)_2\text{S}_2\text{O}_8$ (APS) and ethanol were purchased from Sigma-Aldrich. All chemicals were used as an analytical reagent grade and without further purification. Deionized water was used in all experiments.

2.2 Synthesis of graphene oxide and reduced graphene oxide

Graphene oxide (GO) was synthesized from natural graphite powder by modified Hummer's method, as described elsewhere [23, 24]. 1.5 g of GO was dispersed in 50 ml of double distilled water and sonicated for 30 min. Then 5 ml of hydrazine hydrate was added drop wise to the dispersed suspension and it was heated at 100 °C for 5 h. At that time, a hollow globule of gas was evolved indicating that GO was converted into reduced graphene oxide (RGO). The obtained product was washed several times with 1M HCl and deionized water and dried in an oven at 300 °C for 5 h.

2.3 Synthesis of RGO–CZO/PANI hybrid composite

About 5.94 g of zinc nitrate (0.5 M) and 0.5 g of RGO were dispersed in 50 ml of distilled water. The above mixed suspensions were located in an ice water bath and the reaction temperature was maintained at below 5 °C and stirred for

30 min. Then slowly 3M sodium hydroxide solution was added to the mixed solution, white product formed first, after addition of NaOH, the white product disappeared and the mixed RGO contained $[\text{Zn}(\text{OH})_4]^{2-}$ solution was transparent again. During stirring, 0.1M cobalt nitrate aqueous solution was slowly added to the RGO contained $[\text{Zn}(\text{OH})_4]^{2-}$ solution, precipitate was regenerated and the reaction temperature was maintained at 80 °C. After 6 h, the resulting product was filtered and washed several times with distilled water and ethanol separately. The sample was designated as beaker [A]. Then separately aniline hydrochloride (0.5 ml of aniline in 0.5M HCl) was polymerized with $(\text{NH}_4)_2\text{S}_2\text{O}_8$ in ice bath for 1h, which is labeled beaker [B]. Finally, earlier synthesized beaker [A] was slowly poured into the beaker [B] with stirring for 30 min. Then the whole solution was maintained at 0 °C for 12 h without stirring to complete the chemical reaction. The final dark green product was washed several times with deionized water and ethanol separately and dried in an oven at 80 °C. The sample was designated as RGO–CZO/PANI. Scheme 1 shows the schematic representation of RGO–CZO/PANI hybrid composite synthesis process. For comparison purpose RGO–ZnO, RGO–CZO, RGO/PANI and RGO–ZnO/PANI were synthesized by a similar manner.

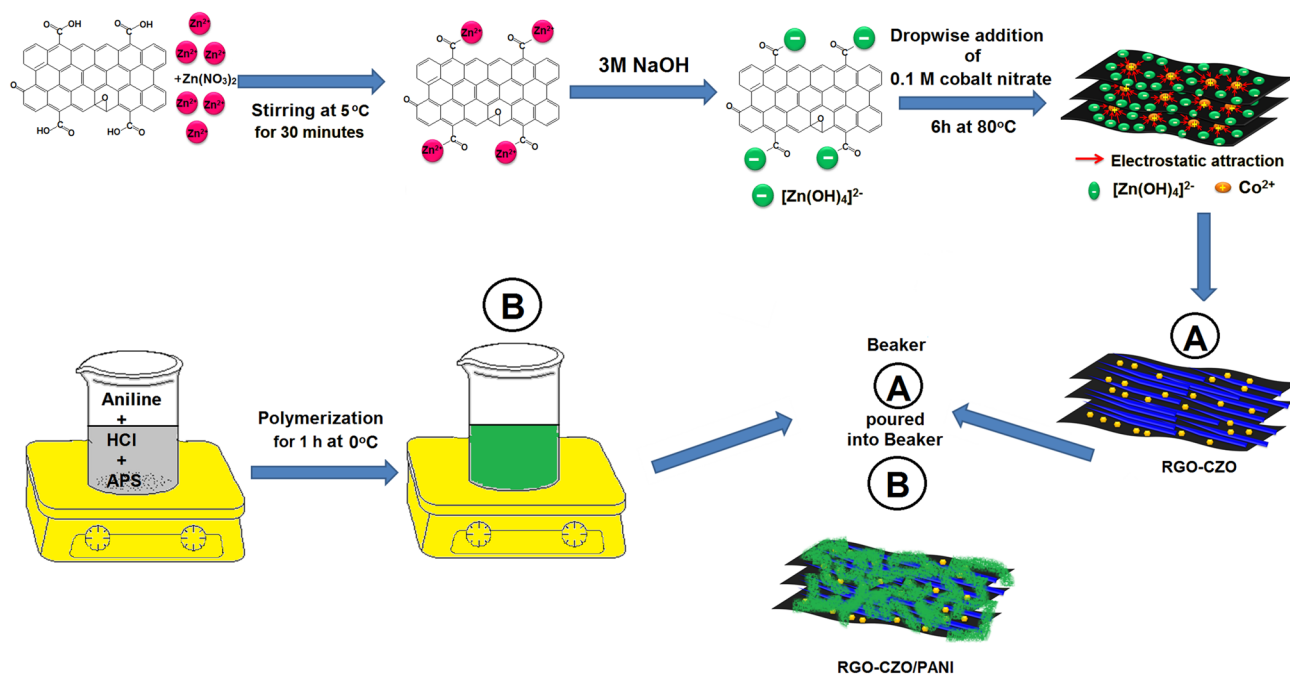
2.4 General characterization

The surface morphology and elemental analysis of the samples were investigated by an HR-SEM coupled with

EDXA, FEI- quanta FEG 250. Nanostructures of the composites were investigated by a TEM analysis (FEG-TEM 300 kV). The crystallographic structures and phase formation of samples were analyzed by powder X-ray diffraction technique using a X'PERT-PRO model with Cu $K\alpha$ radiation sources ($\lambda=0.15406$). The functional group determination was performed by FTIR spectroscopy (FT-IR, SHIMADZU, using KBr pellets) in the range of 4000–450 cm^{-1} . UV–Vis spectra were recorded on a Shimadzu 2401 spectrometer along the composites dispersed in N-methyl-2-pyrrolidone solution (NMP).

2.5 Electrochemical characterization

Electrochemical properties of the hybrid composites were examined (CH instrument model AUTOLAB CHI1102A) in 1M H_2SO_4 solution by cyclic voltammetry, impedance spectroscopy and galvanostatic charge/discharge. To prepare working electrode, slurries made from synthesized hybrid composites were used as the illustrative material, acetylene black as the conductive agent and poly (vinylidene fluoride) as the binder. They were mixed in a weight ratio of 80:10:10 in N-methyl-2-pyrrolidone solvent and coated on a stainless steel with an effective area of 1 cm^2 using a doctoral blade. Before the electrochemical test, the electrode was soaked in 1M H_2SO_4 solution overnight. Electrochemical characterization was carried out in a three-electrode system. A platinum foil and a saturated calomel electrode (SCE) were used as the counter and



Scheme 1 Schematic representation of RGO–CZO/PANI hybrid composite synthesis process

reference electrodes, respectively. The voltage range for CV test varied from -0.2 to 1.0 V with the different scan rates of 20 to 100 mVs^{-1} , while the galvanostatic charge/discharge testing was performed from -0.2 to 1.0 V at the current density from 1 to 5 A g^{-1} . EIS measurements for the composites were recorded in the AC frequency range from 0.01 Hz to 100 kHz at open circuit potential with AC voltage amplitude of 10 mV. A two-electrode system was further employed to obtain more accurate results about the capacitance of as-prepared electrode material using galvanostatic charge/discharge between two symmetrical working electrodes with a polypropylene 2320 as separator in $1\text{M H}_2\text{SO}_4$ aqueous solution. Before electrochemical measurements, all electrodes were first immersed in $1\text{M H}_2\text{SO}_4$ solution for 2 h.

3 Results and discussion

3.1 XRD

Typical XRD pattern of as-synthesized hierarchical structure of RGO, RGO–ZnO, RGO–CZO, RGO/PANI, RGO–ZnO/PANI and RGO–CZO/PANI hybrid composites are shown in Fig. 1. The XRD patterns of the pristine RGO (Fig. 1a) revealed an intense, sharp peak centered at $\approx 25.3^\circ$ confirms the existence of an individual graphene sheet with a stacking structure of the plane (002), which is consistent with the reported reference result [25]. The XRD pattern of RGO–ZnO is shown in Fig. 1b. The corresponding X-ray diffraction peaks for (100), (002) and (101) planes confirm the formation of the wurzite structure of ZnO (JCPDS card No: 36-1451). It indicates the pure phase formation of ZnO without any impurity [26]. The XRD pattern (Fig. 1c) of the RGO–CZO hybrid composite can be indexed to the previously discussed wurzite structure of ZnO pattern as well as the Co_2O_3 peak is observed in the planes at (511) and (440), which is consistent with the H. Yang group reported work result [27]. In addition, the peak intensity has been narrowed for the Co doped composite as compared to the undoped RGO–ZnO. The appeared new peaks confirmed that the Co^{2+} ions are successfully incorporated into the ZnO lattice at the Zn^{2+} sites [28]. For RGO/PANI (Fig. 1d), two broad peaks centered at $2\theta = 20.15$ and 25.26° are corresponding to (020), (200) crystal planes of PANI (periodicity parallel and perpendicular to PANI chains), respectively [29, 30]. Figure 1e, f shows that XRD patterns of RGO–ZnO/PANI and RGO–CZO/PANI hybrid composite, which are different from that of RGO–PANI and they should be related to the presence of metal oxides. These changes will play crucial role in the competition between the localization of the electronic charge to a single chain and delocalization of the charge within the

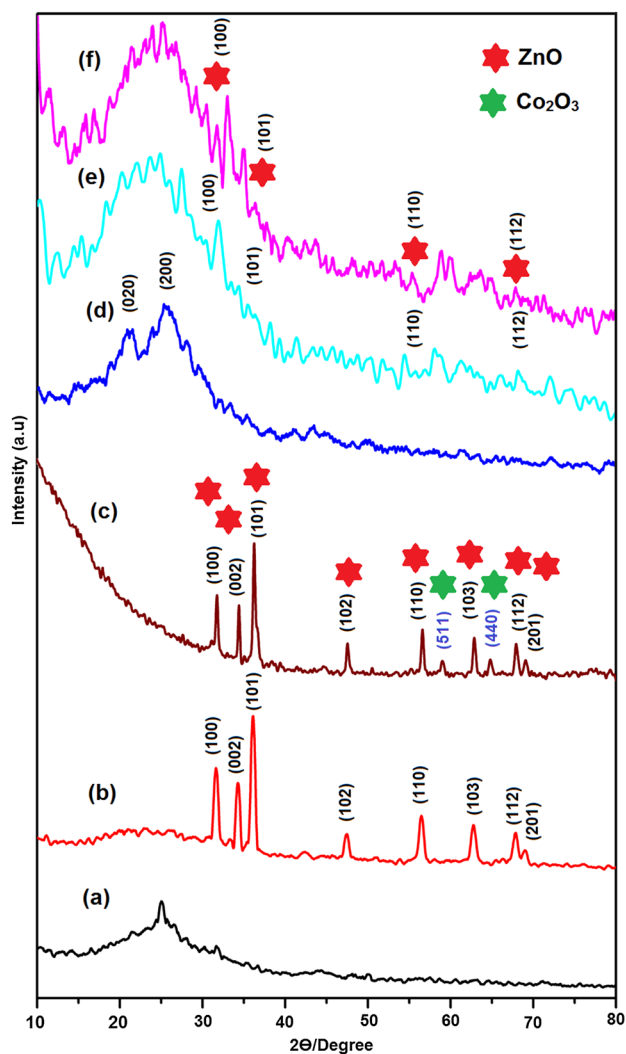


Fig. 1 XRD patterns of (a) RGO, (b) RGO–ZnO, (c) RGO–CZO, (d) RGO/PANI, (e) RGO–ZnO/PANI and (f) RGO–CZO/PANI hybrid composites

three-dimensional amorphous structure [31]. The amorphous structure is beneficial for electrolyte infiltration and cation diffusion.

3.2 FTIR

The FTIR spectra of RGO, RGO–ZnO, RGO–CZO, RGO/PANI, RGO–ZnO/PANI and RGO–CZO/PANI hybrid composites are shown in Fig. 2. The major peaks in FT-IR spectrum of RGO (Fig. 2a) are 1066 , 1616 , 1753 and 3460 cm^{-1} . These peaks are attributed to alkoxy (C–O), aromatic (C=C), carbonyl (C=O) and O–H stretches respectively [32, 33]. The FTIR spectrum of RGO–ZnO (Fig. 2b) shows bands at 481 , 1054 , 1604 and 3494 cm^{-1} corresponding to Zn–O stretching vibration, alkoxy C–O stretching, C=C stretching of the aromatic carbon ring and

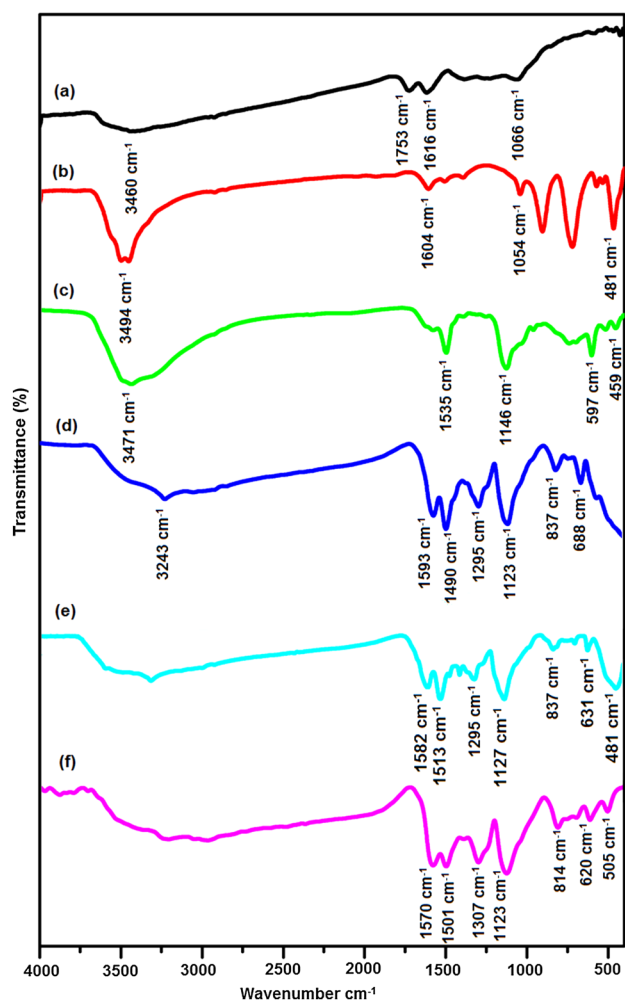


Fig. 2 FTIR spectra of **a** RGO, **b** RGO–ZnO, **c** RGO–CZO, **d** RGO/PANI, **e** RGO–ZnO/PANI and **f** RGO–CZO/PANI hybrid composites

O–H stretching respectively. This result is in good agreement with the previously reported H. N. Tien group's result [34]. Above results confirm the ZnO particles are well incorporated on the RGO sheets. In the RGO–CZO (Fig. 2c) spectrum shows the band at 1146, 1533 and 3471 cm^{-1} corresponding to C–O, C=C and O–H stretching respectively. In addition, it shows strong absorption peaks at 597 and 459 cm^{-1} which corresponds to Co_3O_4 and ZnO peaks respectively [35]. This result is consistent with the XRD results.

The FTIR spectrum of RGO/PANI (Fig. 2d) shows the band at 1593 and 1490 cm^{-1} attributed to the stretching vibration of quinone and benzene rings respectively. The band at 1295 and 1123 cm^{-1} corresponds to the C–N stretching vibration and N=Q=N (where Q=represents the quinoid ring) respectively, indicating HCl doped PANI formed in our samples [36]. The in-plane and out-of-plane bending of C–H stretching of PANI are manifested

837 and 688 cm^{-1} , respectively [37]. The FTIR spectra of RGO–ZnO/PANI (Fig. 2e) and RGO–CZO/PANI (Fig. 2f) hybrid composites represent the major PANI characteristic peaks with slight variation when compared with the RGO/PANI peaks. However the ZnO peak is appeared at 481 cm^{-1} for RGO–ZnO/PANI and after loading of Co ions the band shifted to higher wave number at 505 cm^{-1} for RGO–CZO/PANI. This result clearly confirmed the successful formation RGO–CZO/PANI hybrid composite.

3.3 SEM

Figure 3 shows the SEM images of RGO, RGO–ZnO, RGO–CZO, RGO/PANI, RGO–ZnO/PANI and RGO–CZO/PANI hybrid composites. Figure 3a shows that the RGO material consists of randomly aggregated ultra-fine few layers crumbled sheets that are closely associated with each other one by one. Due to the chemical reduction of GO expanded and large oxygen functional groups decomposed to form very fine and few layer sheets [38, 39]. The RGO–ZnO (Fig. 3b) composite possess grains and a porous structure [40]. It was evident that the electrostatic attraction formed between the negatively charged RGO sheets and positively charged Zn^{2+} in the precursors, which played an important role in the firm attachment of ZnO particles on the RGO sheet to form grains and porous structure [41, 42]

The morphology of RGO–CZO particles are shown in Fig. 3c. From this image rod like particles are viewed and it can be clearly observed that the Co doping changed the morphology of RGO–ZnO. This may be due to the fact that, Co may start to occupy or substituted by interstitial sites of nearby Zn atoms [43]. This behavior is possible due to the small difference in radii of Co_2O_3 (0.58 Å) and ZnO (0.60 Å) [44].

The structure of the synthesized RGO/PANI (Fig. 3d) composite appears to consisting of interconnected, uniform worm-like morphology with five micrometers. The RGO–ZnO/PANI (Fig. 3e) hybrid composite possesses grains and sponge-like morphology. The RGO–CZO/PANI (Fig. 3f) hybrid composite exhibits closely connected needle like structure. It also retains the RGO–CZO composite structure after polymerization reaction. The contact of PANI with metal oxide may be favorable for the enhancement of the electrochemical performance.

3.4 TEM

The TEM image of RGO, RGO–ZnO, RGO–CZO, RGO/PANI, RGO–ZnO/PANI and RGO–CZO/PANI hybrid composites are displayed in Fig. 4. The morphology of RGO (Fig. 4a) shows a wrinkled sheet like structure. In the case of RGO–ZnO (Fig. 4b), it is clearly evident that ZnO particles are decorated in RGO sheets within the scale of

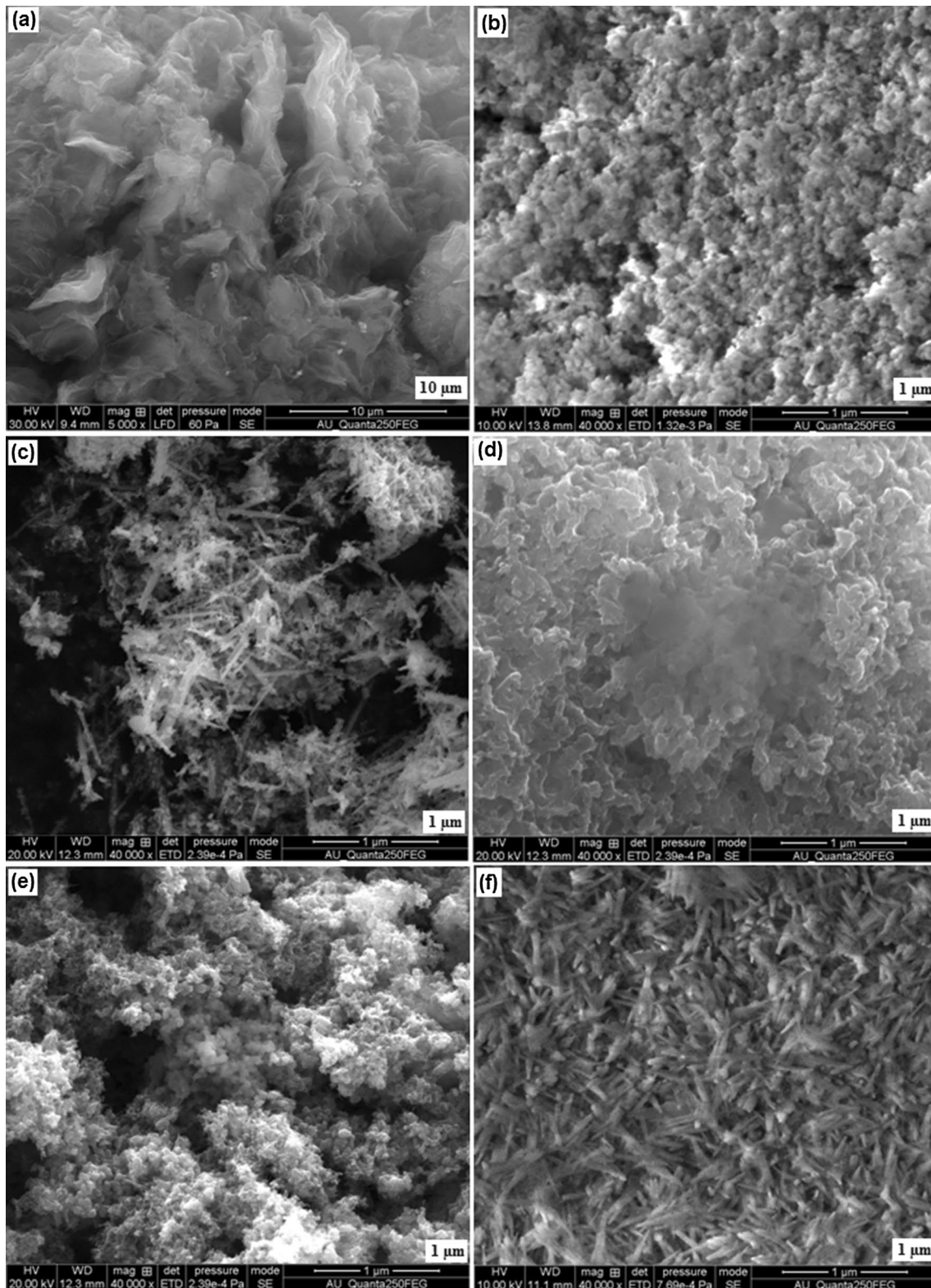


Fig. 3 SEM images of **a** RGO, **b** RGO–ZnO, **c** RGO–CZO, **d** RGO/PANI, **e** RGO–ZnO/PANI and **f** RGO–CZO/PANI hybrid composites

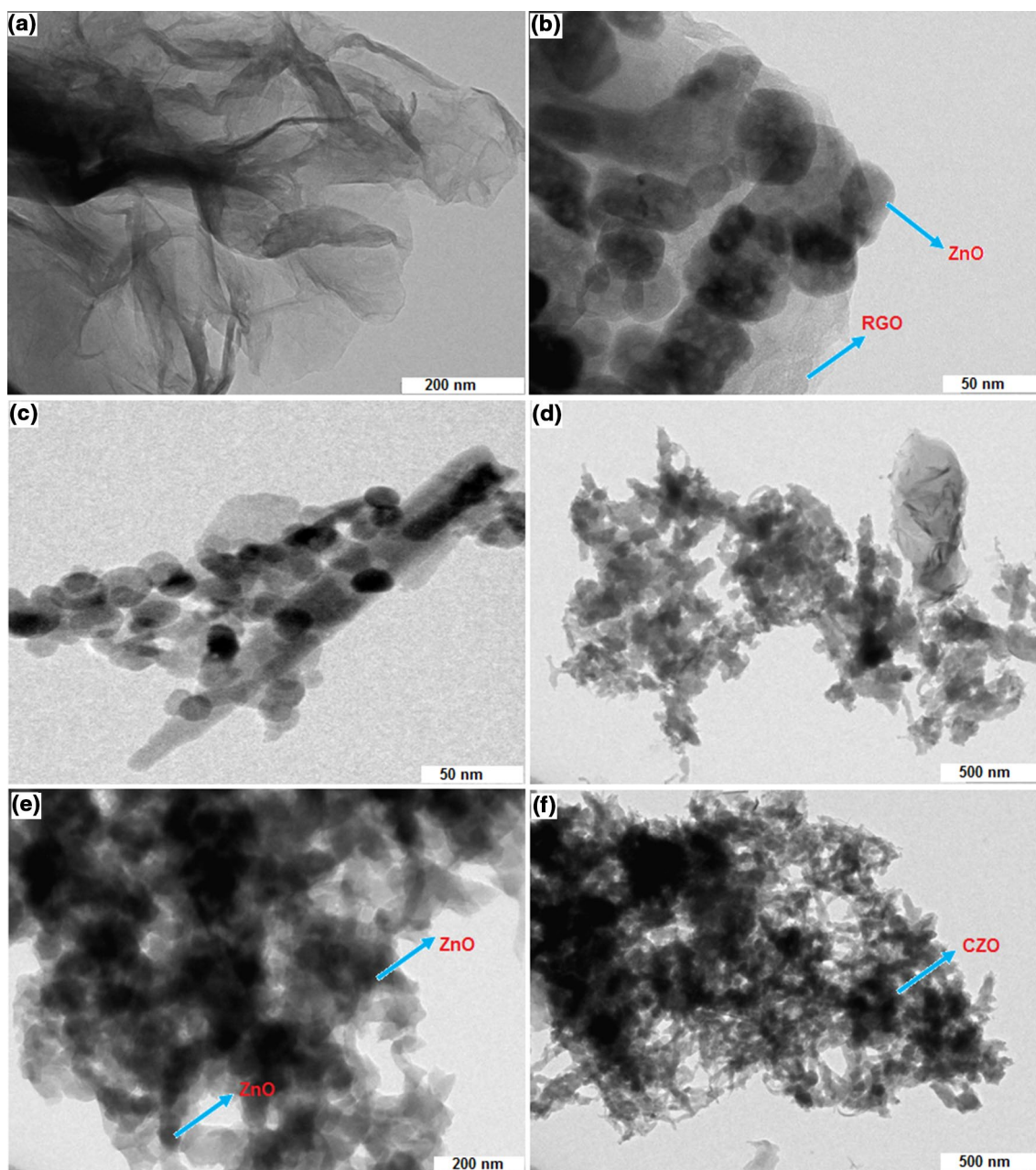


Fig. 4 TEM images of **a** RGO, **b** RGO–ZnO, **c** RGO–CZO, **d** RGO/PANI, **e** RGO–ZnO/PANI and **f** RGO–CZO/PANI hybrid composites

50 nm. The TEM image of RGO–CZO (Fig. 4c) shows rod like structure within the scale of 50 nm. Addition of cobalt ions into the system produce more number of nanorods, which was clearly observed from TEM image. It is interesting to note that the similar morphology was observed in previous discussed SEM analysis result. The nanostructure of RGO/PANI (Fig. 4d) shows both wrinkled sheets and core–shell structures. It is well known that RGO sheets are a good electron acceptor and aniline is a very good electron donor [45]. HCl is used as a dopant, therefore, the monomer of positively charged aniline is to be absorbed onto the

surface of negatively charged RGO sheets through the electrostatic attraction and by the formation of weak charge-transfer complexes between the aniline monomer and the graphitic structure of RGO [46]. Finally the result of this absorption process, RGO sheets are strongly connected by PANI particles by the chemical polymerization process. It was found that the morphology of the RGO–ZnO/PANI (Fig. 4e) changed to an accumulated core–shell structure which is shown dark and bright areas in the image. The dark portion denotes the ZnO nanoparticles, while bright area represents the PANI matrix [47]. This dissimilarity

in the image is due to the difference in the intensity of the radiation when it is passing through the inorganic and organic moieties [48]. The TEM image of RGO–CZO/PANI (Fig. 4f) hybrid composite revealed a rod shaped aggregated structure. The PANI particles contribute to the form of the network, which can interconnect the metal oxide particles, so that the electrons can be readily diffused to the sites where redox reactions take place and can facilitate easy and fast ion/electron transport between the electrode and electrolyte, which are an essential for achieving enhanced electrochemical performance [49].

3.5 UV–Visible spectroscopy analysis

To examine the mid gap state availability of the polymeric composites affected by charge transfer, the UV–Vis spectra

was performed for the composites in NMP at the concentration of 0.1 mg/ml. UV–vis absorption spectra of RGO/PANI, RGO–ZnO/PANI and RGO–CZO/PANI hybrid composite are shown in Fig. 5a. The UV–vis spectrum of RGO/PANI shows three dominated peaks at 283, 335 and 560 nm.

These three peaks are ascribed to the excitation of nitrogen in the benzenoid segments (π – π^* transition), polaron– π^* and n – π^* electronic transitions in the emeraldine salt form of PANI [50]. For the other two composites (RGO–ZnO/PANI and RGO–CZO/PANI) shows two absorption peaks that are shifted when compared with RGO/PANI. The shifting of peaks evidenced the delocalization of charge through PANI chain [51].

The optical absorption spectrum of RGO/PANI, RGO–ZnO/PANI and RGO–CZO/PANI hybrid

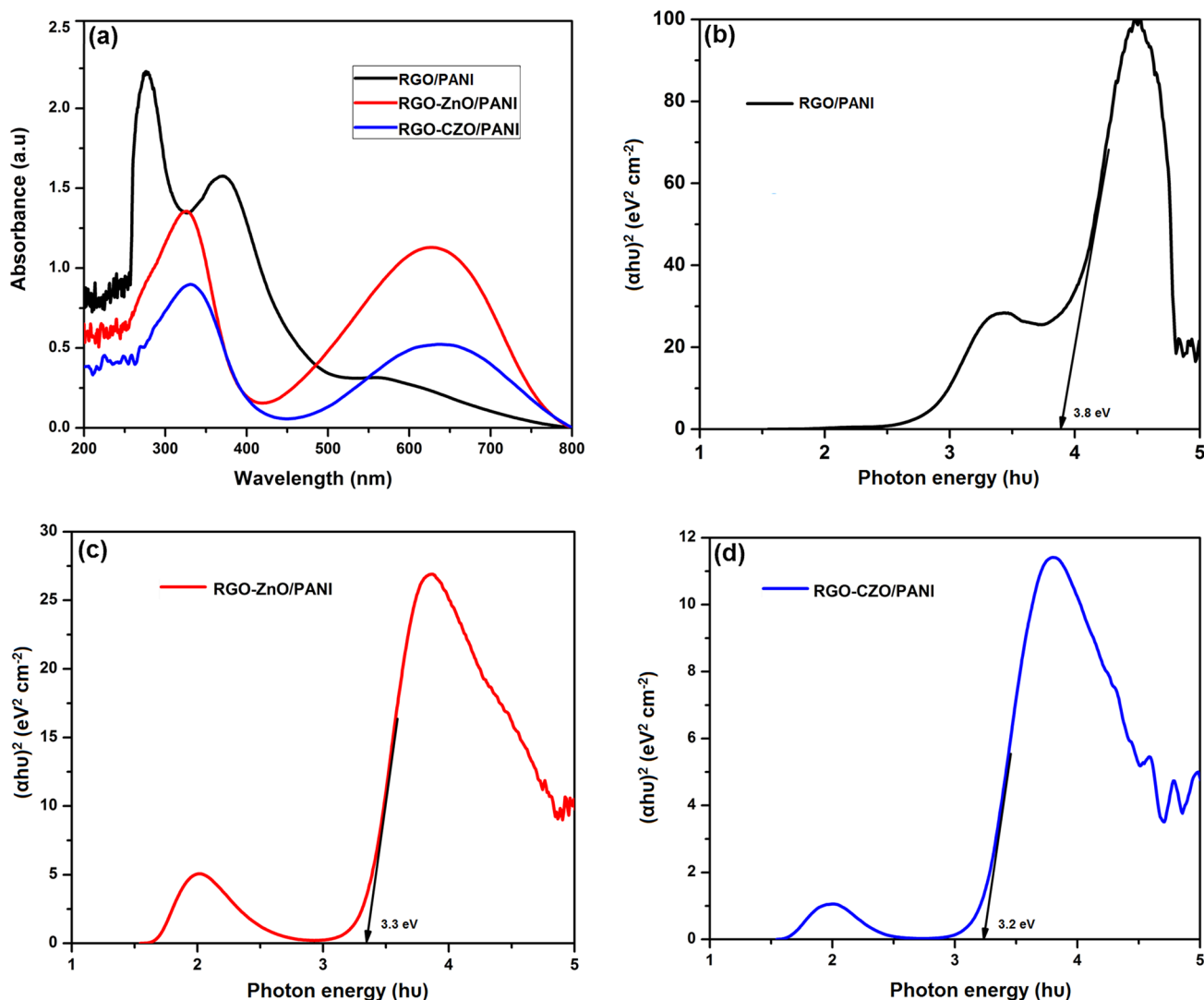


Fig. 5 a UV–Vis spectra of RGO/PANI, RGO–ZnO/PANI and RGO–CZO/PANI hybrid composite. b–d Optical band gap curves of RGO/PANI, RGO–ZnO/PANI and RGO–CZO/PANI hybrid composites

composites (Fig. 5b–d) were obtained and studied to evaluate the absorption coefficient (α) energy gap (E_g), photon energy ($h\nu$) and nature of transition involved, which can be written as below equation [52].

$$\alpha h\nu = A(h\nu - E_g)^n \quad (1)$$

where “ E_g ” is the band gap energy of the materials and “ A ” is a constant and it is different for different transitions, “ $h\nu$ ” is the energy of the photon and “ n ” is an index which assumes the values 1/2, 3/2, 2, and 3 depending on the transition. When $n=1/2$, which implies the direct and allowed transitions. $n=3/2$ which denotes the direct but forbidden. In the case of $n=2$ indicates the indirect and allowed transitions and $n=3$ or more for forbidden cases. Of these $n=1/2$ direct allowed transition equation can be written as:

$$\alpha h\nu = A(h\nu - E_g)^{1/2} \quad (2)$$

From this equation, the band gap was found to be 3.2 eV for RGO–CZO/PANI hybrid composite, 3.3 eV for RGO–ZnO/PANI, 3.8 eV for RGO/PANI. The shift of the band gap additionally confirmed that the metal ions firmly bind with PANI chain as well as RGO. We are known that the metal-polymer interfaces have different Fermi levels (E_F). The electrons are carrying only charges; the balance between donor-receiver is only keeping the E_F level in the semiconductor [53]. So, ion transport phenomenon was occurring between RGO and PANI through the metal coordinate bonding [54]. The reduced optical band gap enhances the electrical behavior of the RGO–CZO/PANI hybrid composite material.

3.6 Electrochemical performances

The potential application of these samples as electrode materials for supercapacitor was tested by standard CV, EIS and GCD method. The CV curves for the RGO/PANI, RGO–ZnO/PANI and RGO–CZO/PANI hybrid composite electrodes are presented in Fig. 6a at a scan rate of 10 mV s^{-1} in the potential window of -0.2 – 1.0 V using $1 \text{ M H}_2\text{SO}_4$ as electrolyte. It can be seen from Fig. 6a, the RGO/PANI, RGO–ZnO/PANI and RGO–CZO/PANI hybrid composite electrodes exhibit redox peaks which indicate all the electrodes have pseudocapacitive behavior.

It is worthy of note that the large loop area of the CV curve of RGO–CZO/PANI is larger than those of other two electrodes at the same scan rate. It is known that the specific capacitance is proportional to the integral area of CV curves, suggesting its enhanced specific capacitance. This improved electrochemical performance can be described as follows: The RGO–CZO/PANI hybrid composite lead to an easy and rapid penetration of the electrolyte ions, which indicates enriching the charge transport between the electrode and electrolyte interface. The superior electrochemical behavior of RGO–CZO/PANI hybrid composite is attributed to the significant synergistic effect of the RGO, Co doped ZnO and PANI. In addition the Co ion inclusion not only improves the double layer capacitance but also improve the pseudo capacitance by increasing the accessible surface area of the hybrid composite. The rate capability for the RGO–CZO/PANI hybrid composite electrode is an important factor. Therefore, the rate properties of RGO–CZO/PANI hybrid composite electrode at different scanning rates are also shown in the range from 20 to

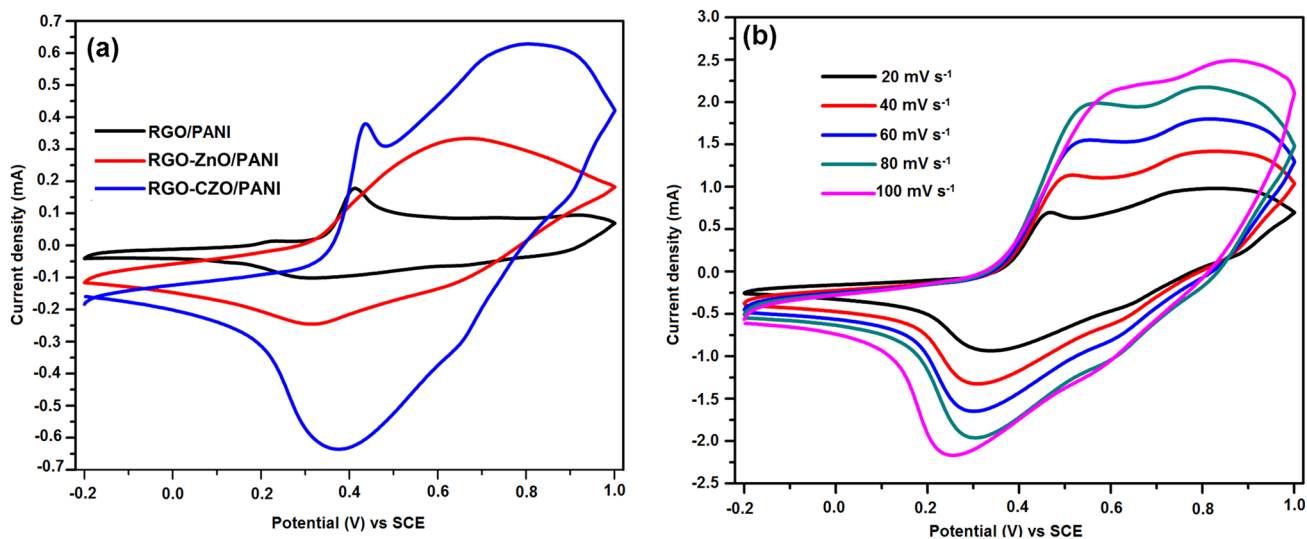


Fig. 6 **a** CV curves of RGO/PANI, RGO–ZnO/PANI and RGO–CZO/PANI electrodes in $1 \text{ M H}_2\text{SO}_4$ at a scan rate of 10 mV/s vs SCE. **b** Different scan rate curves of RGO–CZO/PANI electrode

100 mV s⁻¹ in Fig. 6b. It is seen that the CV curves display similar shapes as the scanning rate increased. The noticeable increase of peak current with a scan rate means that there is a good kinetic process of electrolyte ion diffusion in their pores for the electrode.

The galvanostatic charge–discharge was used to evaluate the capacitive property of RGO/PANI, RGO–ZnO/PANI and RGO–CZO/PANI electrode materials under various current densities. As shown in Fig. 7, the galvanostatic charge–discharge curves of RGO/PANI, RGO–ZnO/PANI and RGO–CZO/PANI electrode materials have a similar symmetrical triangle shape. The symmetrical triangle curves indicate good reversibility of the charge–discharge process. In which all show favorable symmetry and linearity. Furthermore, it was viewed that the discharging time decreasing trend when a higher current density is applied. It clearly denotes that the electrolyte ion cannot penetrate

well into the inner part of active materials due to slow diffusion at higher current density. The specific capacitance (C_{sp}) was calculated with different current densities using the following equations (3).

$$C_{sp} = I \times \Delta t / \Delta V \times m \tag{3}$$

where ‘I’ is the current loaded (A), ‘Δt’ is the discharge time (s), ‘ΔV’ is the potential window change during the discharge process, and ‘m’ is the mass of active material (g) [1]. The calculated specific capacitance values of (from the Eq. 3) RGO–CZO/PANI is 515 F g⁻¹, which is nearly two fold times higher than that of RGO–ZnO/PANI (265 F g⁻¹) and three fold times higher than that of RGO–PANI (169 F g⁻¹). The improvement of capacitive property of RGO–CZO/PANI is attributed to the synergistic effect of the two different mechanisms such as electric double layer capacitor and Faradic pseudocapacitor.

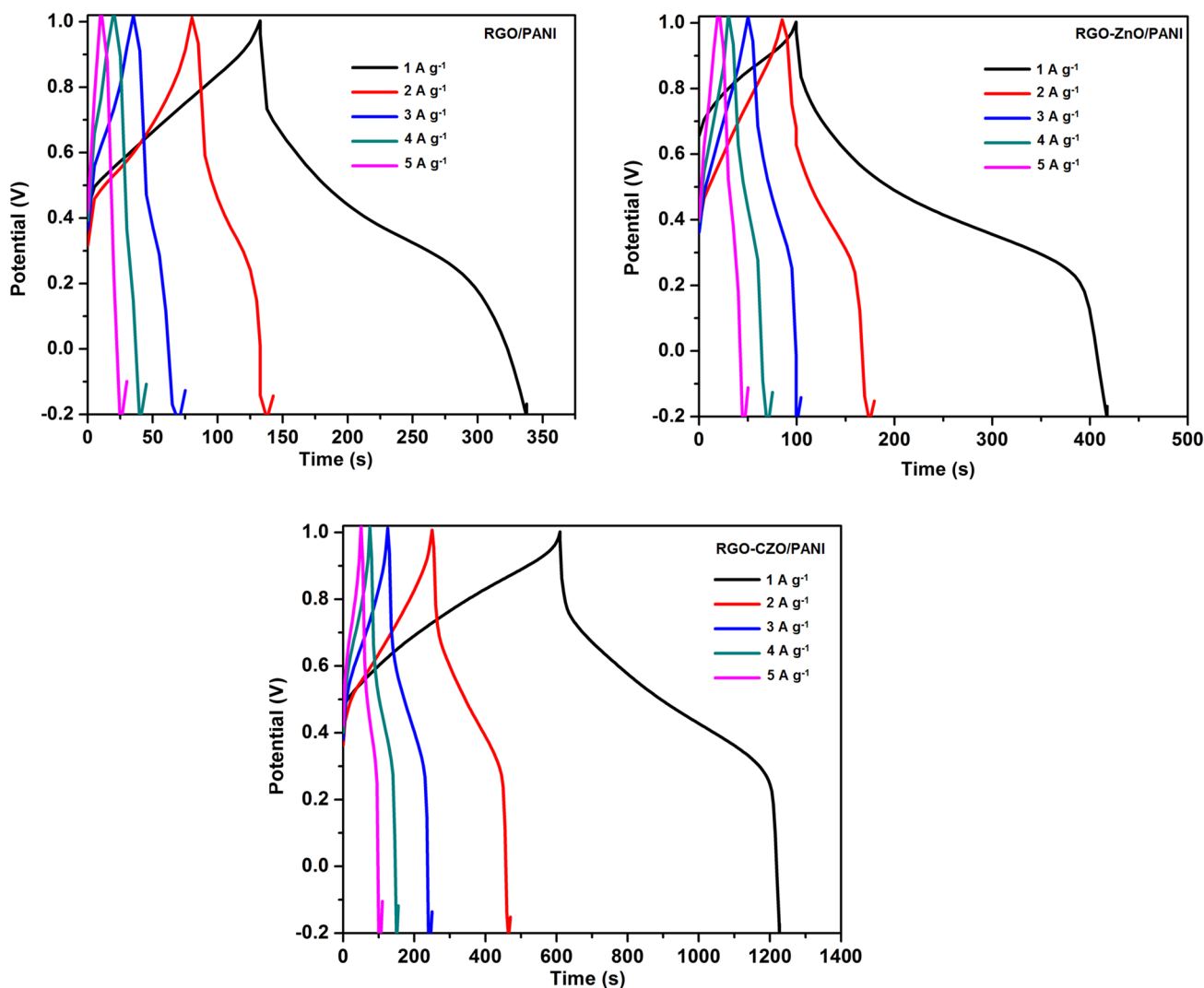


Fig. 7 Charge discharge curves of RGO/PANI, RGO–ZnO/PANI and RGO–CZO/PANI electrodes at various current densities (1, 2,3,4,5 Ag⁻¹)

Electrochemical impedance spectroscopy study has been recognized as one of the principal techniques for investigating the electron and ion transport in electrode material. The charge transfer resistance (R_{ct}) value of the RGO/PANI, RGO-ZnO/PANI and RGO-CZO/PANI were calculated from the EIS over the frequency range of 0.01 Hz–100 kHz using three electrode systems in 1M H_2SO_4 solutions using sinusoidal wave amplitude of 10 mV at the high frequency region as shown in Fig. 8a. The RGO/PANI, RGO-ZnO/PANI and RGO-CZO/PANI hybrid composite electrodes are similar composed of semicircle at high frequency region, which gives solution resistance (R_s) and charge transfer resistance (R_{ct}). Warburg impedance was viewed from the project line (45°) at the low frequency region and it displays the diffusive resistance of electrolyte ions in host materials. The R_{ct} values of RGO/PANI, RGO-ZnO/PANI

and RGO-CZO/PANI hybrid composite electrodes were calculated from EIS (Fig. 8a) and values found to be 748, 445 and 185 Ω respectively. The R_{ct} value of RGO-CZO/PANI electrode is lower than that of RGO-ZnO/PANI electrode, so there is an unrestricted charge transfer possessing in RGO-CZO/PANI. Hence, EIS study shows good electrochemical behavior for RGO-CZO/PANI compared to RGO-ZnO/PANI.

Figure 8b represents the current densities versus specific capacitance (C_{sp}) curves for RGO/PANI, RGO-ZnO/PANI and RGO-CZO/PANI hybrid composite electrodes. All materials have linear plots with decreased current density and increased the specific capacitance. The maximum specific capacitance (C_{sp}) values of RGO/PANI, RGO-ZnO/PANI and RGO-CZO/PANI materials are 169, 265 and 515 $F\ g^{-1}$ for the current density of 1 $A\ g^{-1}$ respectively.

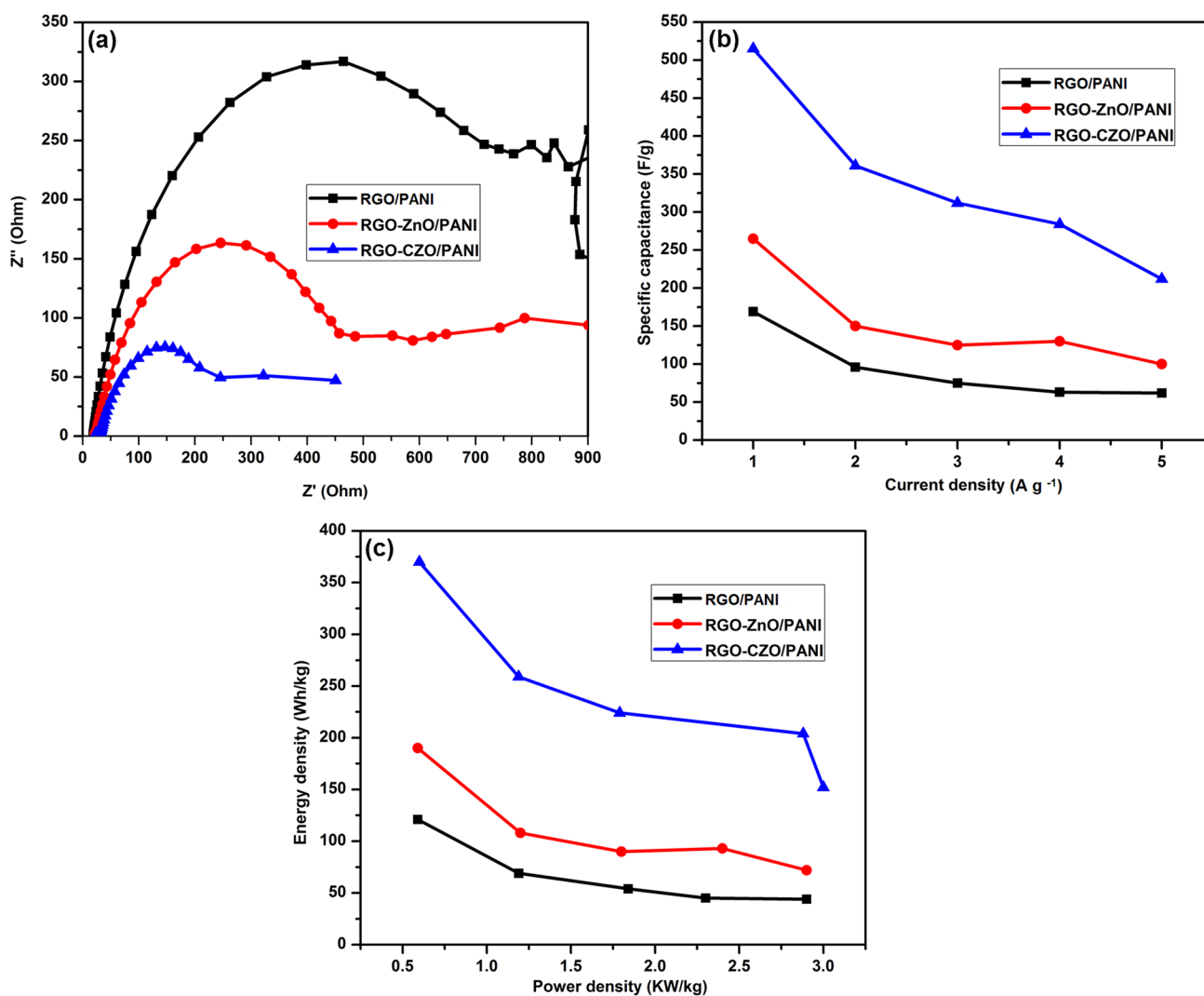


Fig. 8 a Impedance spectra of RGO/PANI, RGO-ZnO/PANI and RGO-CZO/PANI electrodes. b Specific capacitance curves of RGO/PANI, RGO-ZnO/PANI and RGO-CZO/PANI electrodes. c Ragone plot curves of RGO/PANI, RGO-ZnO/PANI and RGO-CZO/PANI electrodes

The RGO–CZO/PANI hybrid composite electrode showed almost twice the specific capacitance of RGO–ZnO/PANI and it shows the good capacitive performance for supercapacitor energy storage applications. The specific capacitance values obtained for this synthesized RGO–CZO/PANI hybrid composite electrode is larger or comparable with the values reported in a previous published work (Table 1)

Figure 8c depicts the Ragone plots for RGO/PANI, RGO–ZnO/PANI and RGO–CZO/PANI samples to evaluate the energy density and power density for supercapacitor applications. The energy (E) and power density (P) was calculated using the following equations [63].

$$E = 1/2CV^2 \tag{4}$$

$$P = E/t \tag{5}$$

where, ‘E’ is the energy density (Wh/kg), ‘C’ is the specific capacitance (F/g), ‘V’ is the discharge potential (V), ‘P’ is the power density (KW/kg) and ‘t’ is the discharging time (s). The RGO–PANI electrode can deliver an energy density in the range of 121–44 Wh kg⁻¹ and power density in the range of 0.59–2.9 kW kg⁻¹. The RGO–ZnO/PANI electrode can provide an energy density in the range of 190–72 Wh kg⁻¹ and power density in the range of 0.6–3 kW kg⁻¹. It was observed that the RGO–CZO/PANI material has high energy density values in the range of 370–152 Wh kg⁻¹, while the power density values are in the range of 0.62–3.1 kW kg⁻¹. The enhanced energy and power density of RGO–CZO/PANI hybrid composite may be due to the synergistic effect between the conducting organic material and inorganic metal oxides. Hence, the RGO–CZO/PANI hybrid composite is a promising electrode material with good capacitance and energy density for super capacitor applications.

The electrochemical performances of RGO/PANI, RGO–ZnO/PANI and RGO–CZO/PANI samples were further studied in this work by a two-electrode cell configuration. Given that the voltage window of 0.0–0.1 V is the most appropriate one for supercapacitors and the results are

displayed in Figs. 9 and 10. Figure 9a shows the CV curves of RGO/PANI, RGO–ZnO/PANI and RGO–CZO/PANI electrode cells. It is obvious that the RGO–CZO/PANI electrode cell shows the highest current density among all the electrodes, implying its best capacitive performance. Figure 9b–d shows the CV curves of RGO/PANI, RGO–ZnO/PANI and RGO–CZO/PANI electrode cells at different scan rates, demonstrating the good rate property and excellent capacitance behavior.

The galvanostatic charge–discharge curves (Fig. 10a) displays slightly distorted triangular shapes at the same current density of 1 A g⁻¹, indicating capacitance performance from the combination of double layer capacitance formation and redox reactions [63]. In addition, we can simply observe that the discharging time of the RGO–CZO/PANI sample has obviously been improved compared with other samples owing to the pseudo-capacitive behavior derived from synergistic contributions of individual components assist charge transport and energy storage. The galvanostatic charge–discharge curves and different current densities of RGO/PANI, RGO–ZnO/PANI and RGO–CZO/PANI are shown in Fig. 10b–d. The shape of the charge–discharge curve deviates largely from linearity, indicating that the charge storage mainly originated from Faradic redox reactions [64]. The specific capacitance of the electrode material is indicated through the discharging time; the longer the discharging duration improves the specific capacitance of the composite material [65]. Based on the discharge curve the specific capacitance of the RGO–CZO/PANI (Fig. 10e) electrode reaches up to 208 F g⁻¹ at 1 A g⁻¹, but the specific capacitance for RGO–ZnO/PANI and RGO/PANI only reach 82 and 22 F g⁻¹ respectively.

The energy density and power density are two key factors to estimate the performance of supercapacitors for practical application. Figure 10f shows the Ragone plot relating the energy density to the power density of symmetric cell. Notably, the energy density decreases with the increase of the current density, while the power density enhances with the increase of the current density [66]. The high energy density achieves 28.88 Wh kg⁻¹ at

Table 1 Specific capacitance comparison of our hybrid composite electrode with previously reported work

Material	Electrolyte	Current density	Specific capacitance (F g ⁻¹)	References
Graphene/PANI	1M H ₂ SO ₄	0.1 A g ⁻¹	257	[55]
Polyaniline/Graphene	1M H ₂ SO ₄	0.25 A g ⁻¹	340	[56]
Layered PANI/Graphene	1M H ₂ SO ₄	0.5 A g ⁻¹	384	[57]
Polyaniline/Graphene oxide	1M H ₂ SO ₄	0.5 A g ⁻¹	355	[58]
Graphene/MnO ₂ /PANI	1M Na ₂ SO ₄	1 A g ⁻¹	305	[59]
Co ₃ O ₄ /MWCNT/GNS	1M NaOH	CV 10 mV s ⁻¹	294	[60]
Graphene/ZnO	1M KCl	CV 5 mV s ⁻¹	109	[61]
RGO-CZO/PANI	1M H ₂ SO ₄	1 A g ⁻¹	515	This work

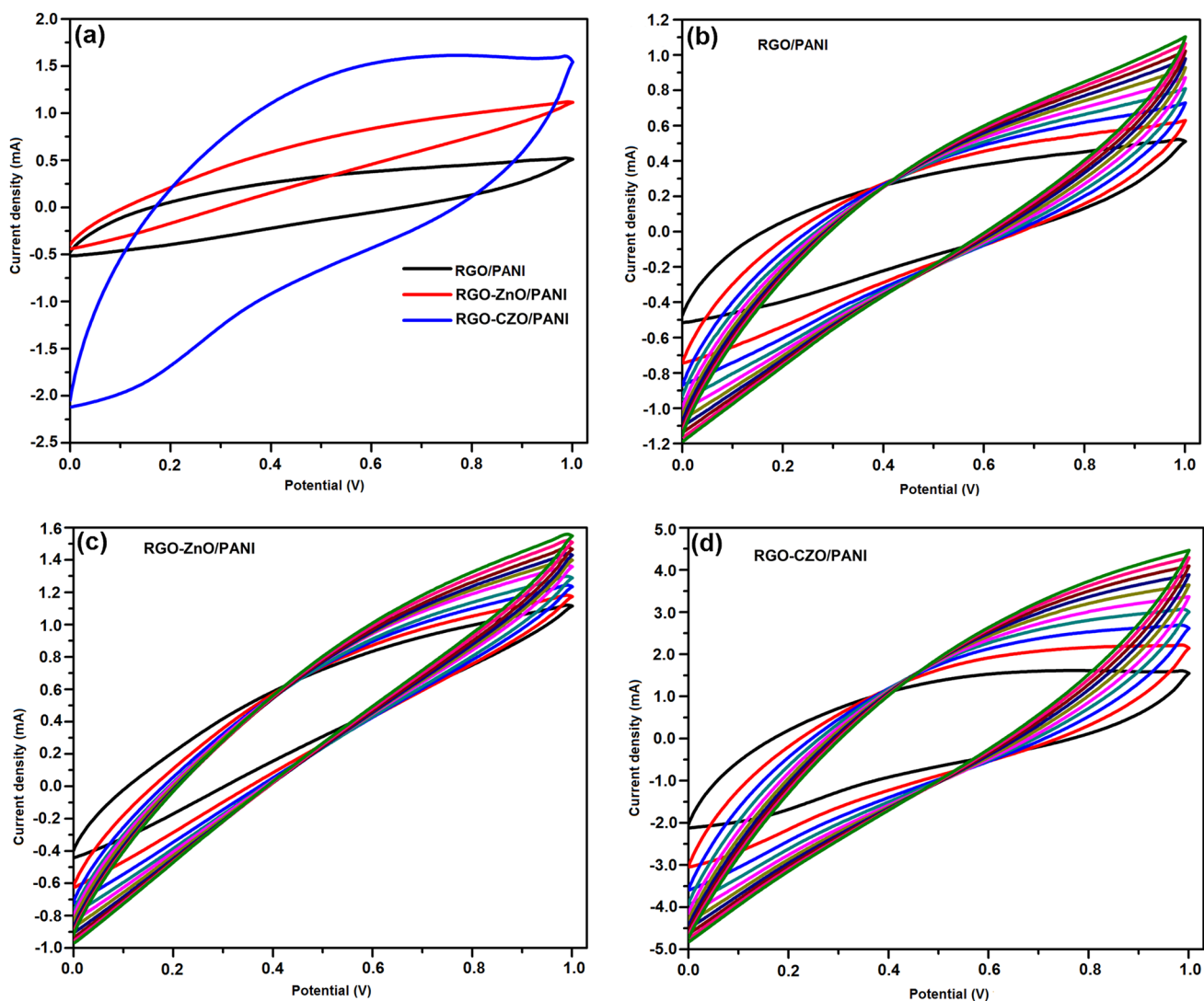


Fig. 9 Electrochemical performances measured by a two electrode system **a** CV curves of RGO/PANI, RGO-ZnO/PANI and RGO-CZO/PANI electrode cells. **b–d** Different scan rates curves of RGO/PANI, RGO-ZnO/PANI and RGO-CZO/PANI electrode cells

a power density of 0.694 kW kg^{-1} in RGO-CZO/PANI, which is much higher than other electrodes such as RGO-ZnO/PANI (11.38 Wh kg^{-1} at 0.595 kW kg^{-1}) and RGO/PANI (3.05 Wh kg^{-1} at 0.494 kW kg^{-1}). The superior energy-storage performance can be ascribed to the following factors. First, the improved electronic conductivity provides quick charge transfer in the hybrid composite electrode. Second, the synergistic contribution of the individual components, such as Co doped ZnO, RGO and PANI. Third, the effective porous network structure provides more response active sites, which is beneficial for rapid ion diffusion and transport to the electrode-electrolyte interface [67].

4 Conclusions

In the present work, RGO-CZO/PANI hybrid composites were synthesized by simple chemical co-precipitation and in situ chemical oxidative polymerization method. A series of characterization methods (XRD, FTIR, SEM, TEM and UV-Vis) were confirmed that PANI has successfully coated the RGO-CZO hybrid composite. It is found that the well-designed hierarchical nanostructure and the synergistic effects among the three components (CZO, RGO and PANI) are conducive to the high electrochemical performance. The fabricated electrode of RGO-CZO/PANI could absorb more electrolyte ions, shorten the electronic path

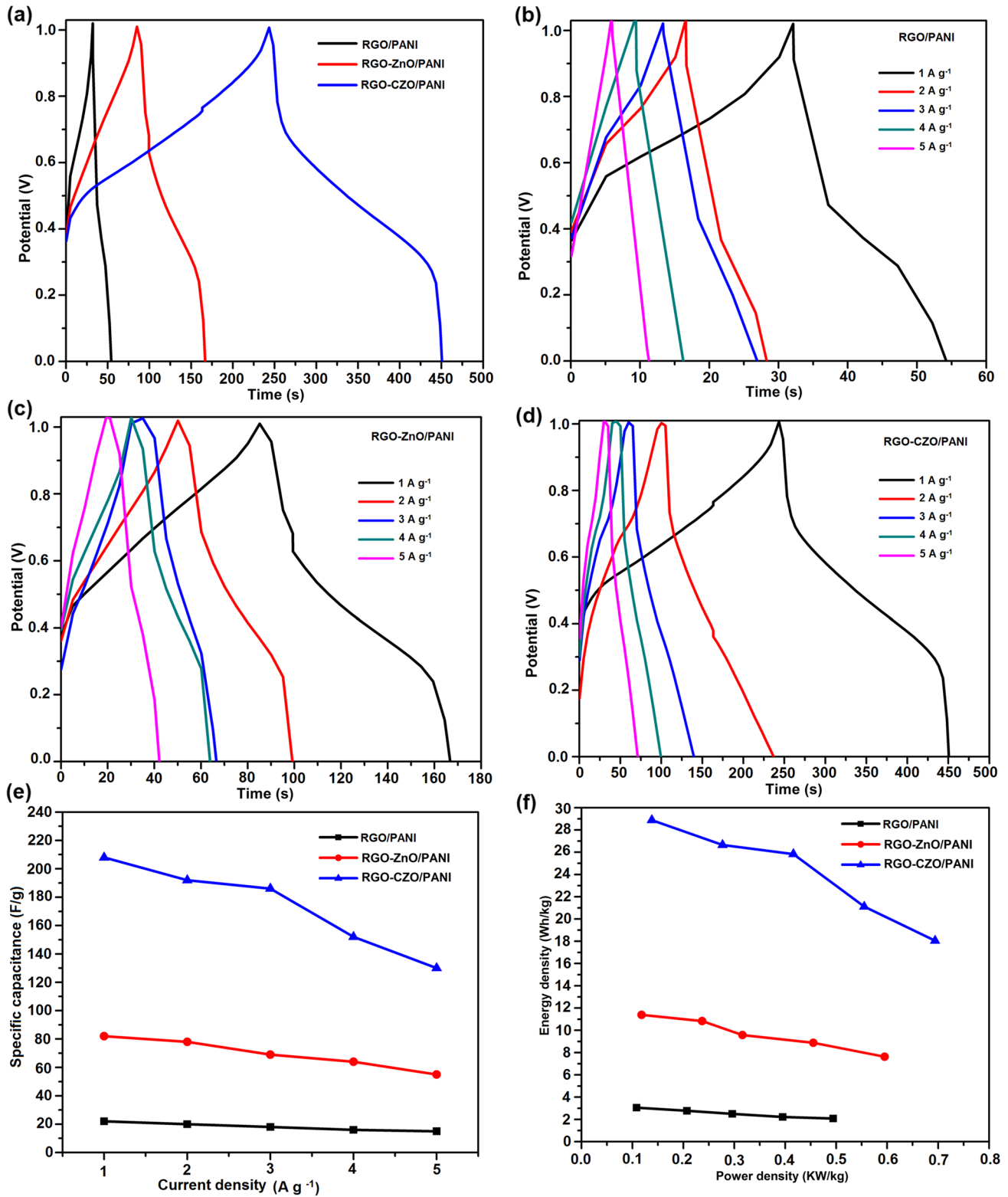


Fig. 10 a Galvanostatic charge–discharge curves of RGO/PANI, RGO–ZnO/PANI and RGO–CZO/PANI supercapacitor cells at a current density of 1 A g⁻¹. b–d Galvanostatic charge–discharge curves of RGO/PANI, RGO–ZnO/PANI and RGO–CZO/PANI electrode

cells at different current density (1, 2,3,4,5 A g⁻¹). e Specific capacitance and f Ragone plots curves of RGO/PANI, RGO–ZnO/PANI and RGO–CZO/PANI electrode cells

length, and promote the usage of active material and leading to the excellent electrochemical performance, which includes a specific capacitance, energy density and power density. The supercapacitors exhibiting superior capacitive performances can be implemented in the voltage windows of -0.2 to 1.0 V and 0.0 to 1.0 V when conducting in a three electrode system (515 F g^{-1}) and two electrode system (208 F g^{-1}), respectively. Therefore, we hope that such designed material could be considered as a perspective electrode material for high performance supercapacitors. Furthermore, the process of forming and relating ideas of constructing stable materials could open up a brand new filed for fabricating supercapacitors.

Acknowledgements The authors would like to thank the University Grants Commission, New Delhi, India, for providing financial assistance from UGC-BSR Fellowship. The author greatly acknowledged the Department of Physics, Alagappa University, Karaikudi for providing XRD (DST-FIST) facilities and Department of Industrial Chemistry, Alagappa University, Karaikudi for providing HR-SEM analysis. I gratefully acknowledge V.Maruthapandian and S.Sathyamoorthi, Research scholars, Central Electrochemical Research Institute, Karaikudi, India for their valuable suggestions during this part of my research work.

References

1. F. Chen, P. Liu, Q. Zhao, *Electrochim. Acta* **76**, 62–68 (2012)
2. H. Javadian, F.Z. Sorkhrodi, B.B. Koutenaeei, *J. Ind. Eng. Chem.* **20**, 3678–3688 (2014)
3. H.W. Wang, Z.A. Hu, Y.Q. Chang, Y.L. Chen, Z.Y. Zhang, Y.Y. Yang, H.Y. Wu, *Mater. Chem. Phys.* **130**, 672–679 (2011)
4. A. Jamil, H.N. Lim, N.A. Yusof, A.A. Tajudin, N.M. Huang, A. Pandikumar, A. Moradi Golsheikh, Y.H. Lee, Y. Andou, *Sens. Actuators B* **221**, 1423–1432 (2015)
5. C.C. Yeh, D.H. Chen, *Appl. Catal. B Environ.* **150**, 298–304 (2014)
6. A. Prakash, D. Bahadur, *ACS Appl. Mater. Interfaces* **6**, 1394–1405 (2014)
7. D.P. Norton, Y.W. Heo, M.P. Ivill, K. Ip, S.J. Pearton, M.F. Chisholm, T. Steiner, *Mater. Today* **7**, 34–40 (2004)
8. M. Norouzi, M. Kolahdouz, P. Ebrahimi, M. Ganjian, R. Soleimanzadeh, K. Narimani, H. Radamson, *Thin Solid Films* **619**, 41–47 (2016)
9. X.H. Xia, J.P. Tu, X.L. Wang, C.D. Gu, X.B. Zhao, *Chem. Commun.* **47**, 5786–5788 (2011)
10. Y. Liang, Y. Li, H. Wang, J. Zhou, J. Wang, T. Regier, H.J. Dai, *Nat. Mater.* **10**, 780–786 (2011)
11. C. Kuang, C. Lin, Y. Lai, R. Vittal, K.C. Ho, *Biosens. Bioelectron.* **27**, 125–131 (2011)
12. P. Poizot, S. Laruelle, S. Grugeon, L. Dupont, J.M. Tarascon, *Nature* **407**, 496–499 (2000)
13. J.W. Xiao, S.H. Yang, *J. Mater. Chem.* **22**, 12253–12262 (2012)
14. W.H. Nam, B.B. Kim, S.G. Seo, Y.S. Lim, J.Y. Kim, W.S. Seo, W.K. Choi, H.H. Park, J.Y. Lee, *Nano Lett.* **14**, 5104–5109 (2014)
15. M.A. Garakani, S. Abouali, B. Zhang, C.A. Takagi, Z.L. Xu, J. Huang, J. Huang, J.K. Kim, *ACS Appl. Mater. Interfaces* **6**, 18971–18980 (2014)
16. N. Karak, B. Pal, D. Sarkar, T.K. Kundu, *J. Alloys Compd.* **647**, 252–258 (2015)
17. L. Li, G. Ruan, Z. Peng, Y. Yang, H. Fei, A. Rahman O. Raji, E.L.G. Samuel, M. J., *Tour. ACS Appl. Mater. Interfaces* **6**, 15033–15039 (2014)
18. T.T. Nguyen, V.H. Nguyen, R.K. Deivasigamani, D. Kharismadewi, Y. Iwai, J.J. Shim, *Solid state sci.* **53**, 71–77 (2016)
19. N. Parvatikar, S. Jain, C.M. Kanamadi, B.K. Chougule, S.V. Bhoraskar, M.V.N. Ambika Prasad, *J. Appl. Polym. Sci.* **103**, 653–658 (2007)
20. V.H. Nguyena, J.J. Shim, *Synth. Metals* **207**, 110–115 (2015)
21. S. Radhakrishnan, K. Krishnamoorthy, C. Sekar, J. Wilson, S.J. Kim, *Chem. Eng. J.* **259**, 594–602 (2015)
22. H. Su, T. Wang, S. Zhang, J. Song, C. Mao, H. Niu, B. Jin, J. Wu, Y. Tian, *Solid State Sci.* **14**, 677–681 (2012)
23. W.S. Hummers, R.E. Offeman, *J. Am. Chem. Soc.* **80**, 1339 (1958)
24. F. Akbar, M. Kolahdouz, Sh. Larimian, B. Radfar, H.H. Radamson, *J. Mater. Sci.* **26**, 4347–4379 (2015)
25. F. Du, W. Yang, F. Zhang, C.Y. Tang, S. Liu, L. Yin, W.C. Law, *ACS Appl. Mater. Interfaces* **7**, 14397–14403 (2015)
26. P. Chand, A. Gaur, A. Kumar, *J. Alloys Compd.* **539**, 174–178 (2012)
27. H. Yang, S. Nie, *Mater. Chem. Phys.* **114**, 279–282 (2009)
28. B. Pal, S. Dhara, P.K. Giri, D. Sarkar, *J. Alloys Compd.* **615**, 378–385 (2014)
29. P. Liu, Y. Huang, L. Wang, W. Zhang, *Synth. Metals* **177**, 89–93 (2013)
30. B. Ma, X. Zhou, H. Bao, X. Li, G. Wang, *J. Power Sources* **215**, 36–42 (2012)
31. X. Li, Y. Chai, H. Zhang, G. Wang, X. Feng, *Electrochim. Acta* **85**, 9–15 (2012)
32. C. Nethravathi, M. Rajamathi, *Carbon* **46**, 1994–1998 (2008)
33. Y. Wang, G. Xia, C. Wua, J. Sun, R. Song, W. Huang, *Carbohydr. Polym.* **115**, 686–693 (2015)
34. H.N. Tien, V.H. Luan, L.T. Hoa, N.T. Khoa, S.H. Hahn, J.S. Chung, E.W. Shin, S.H. Hur, *Chem. Eng. J.* **229**, 126–133 (2013)
35. P. Shi, R. Su, S. Zhu, M. Zhu, D. Li, S. Xu, *J. Hazard. Mater.* **229**, 331–339 (2012)
36. G.D. Prasanna, H.S. Jayanna, V. Prasad, *J. Appl. Polym. Sci.* **120**, 2856–2862 (2011)
37. O. Tovine, N. Jahed, C.E. Sunday, K. Pokpas, R. F. Ajayi, H.R. Makelane, K.M. Molapo, S.V. John, P. G. Baker, E. I. Iwuoha, *Sens. Actuators B* **205**, 184–192 (2014)
38. Y. Zhou, B. Xiao, S.Q. Liu, Z. Meng, Z.G. Chen, C.Y. Zou, C.B. Liu, F. Chen, X. Zhou, *Chem. Eng. J.* **283**, 266–275 (2016)
39. M. Mrlik, M. Ilcikova, T. Plachy, V. Pavlinek, Z. spitalisky, J. Mosnacek, *Chem. Eng. J.* **283**, 717–720 (2016)
40. A. Lamberti, A. Sacco, M. Laurenti, M. Fontana, C.F. Pirri, S. Bianco, *J. Alloys Compd.* **615**, 487–490 (2014)
41. A.S.M. Iftekhar Uddin, G.S. Chung, *Sens. Actuators B* **205**, 338–344 (2014)
42. Y.J. Kim, H. Warman, A. Yoon, M.Y. Kim, G.C. Yi, C.L. Liu, *Nanotechnology* **22**, 245603–245611 (2011)
43. M. Tay, Y.H. Wu, G.C. Han, T.C. Chong, Y.K. Zheng, S.J. Wang, Y.B. Chen, X.Q. Pan, *J. Appl. Phys.* **100**, 063910–063919 (2006)
44. M. Nirmala, A. Anukaliani, *Phys. B* **406**, 911–915 (2011)
45. N. Ashok Kumar, H.J. Choi, Y.R. Shin, D.W. Chang, L. Dai, J.B. Baek, *ACS nano* **6**, 1715–1723 (2012)
46. Q. Wu, Y. Xu, Z. Yao, A. Liu, G. Shi, *ACS nano* **4**, 1963–1970 (2010)
47. J.A. Khan, M. Qasim, B.R. Singh, S. Singh, M. Shoeb, W. Khan, D. Das, A.H. Naqvi, *Spectrochim. Acta Part A* **109**, 313–321 (2013)

48. R. Ramakrishnan, J.D. Sudha, V.L. Reena, RSC Adv. **2**, 6228–6236 (2012)
49. H. Guo, L. Liu, Q. Wei, H. Shu, X. Yang, Z. Yang, M. Zhou, J. Tan, Z. Yan, X. Wang, Electrochim. Acta **94**, 113–123 (2013)
50. S. Bhadra, N. Singha, D. Khastgir, J. Appl. Polym. Sci. **104**, 1900–1904 (2007)
51. D.S. Dhawale, R.R. Salunkhe, V.S. Jamadade, T.P. Gujar, C.D. Lokhande, Appl. Surf. Sci. **255**, 8213–8216 (2009)
52. B.T. Raut, P.R. Godse, S.G. Pawar, M.A. Chougule, D.K. Bandgar, S. Sen, V.B. Patil, J. Phys. Chem. Solids **74**, 236–244 (2013)
53. G.R.F. Edson, A.W.S. Demetrio, A.A.D.Q. Alvar, J. Mater. Sci. **19**, 457–462 (2008)
54. S. Giri, D. Ghosh, C.K. Das, J. Electroanal. Chem. **697**, 32–45 (2013)
55. Z.F. Li, H. Zhang, Q. Liu, L. Sun, L. Stanciu, J. Xie, ACS Appl. Mater. Interfaces **5**, 2685–2691 (2013)
56. L. Li, A.R.O. Raji, H. Fei, Y. Yang, E.L.G. Samuel, M.J. Tour, ACS Appl. Mater. Interfaces **5**, 6622–6627 (2013)
57. Z. Tong, Y. Yang, J. Wang, J. Zhao, B.L. Su, Y. Li, J. Mater. Chem. A **2**, 4642–4651 (2014)
58. D. Gui, C. Liu, F. Chen, J. Liu, Appl. Surf. Sci. **307**, 172–177 (2014)
59. W. Chen, X. Tao, Y. Li, H. Wang, D. Wei, C. Ban, J. Mater. Sci. doi:[10.1007/s10854-016-4632-0](https://doi.org/10.1007/s10854-016-4632-0)
60. T. Battumur, S.B. Ambade, R.B. Ambade, P. Pokharel, D.S. Lee, S.H. Han, W. Lee, S.H. Lee, Curr. Appl. Phys. **13**, 196–204 (2013)
61. A. Ramadoss, S.J. Kim, Mater. Chem. Phys **140**, 405–411 (2013)
62. V. Thirumal, A. Pandurangan, R. Jayavel, R. Ilangoan, Synth. Metals **220**, 524–532 (2016)
63. L. Sun, C.G. Tian, Y. Fu, Y. Yang, J. Yin, L. Wang, H. Fu, Chem. Eur. J. **20**, 564–574 (2014)
64. S. Vijayakumar, S. Nagamuthu, S.H. Lee, K.S. Ryu, Int. J. Hydrog. Energy. doi:[10.1016/j.ijhydene.2016.09.159](https://doi.org/10.1016/j.ijhydene.2016.09.159)
65. C.Y. Foo, H.N. Lim, M.A.b. Mahdi, K.F. Chong, N.M. Huang, J. Phys. Chem. C **120**, 21202–21210 (2016)
66. M. Yan, Y. Yao, J. Wen, L. Long, M. Kong, G. Zhang, X. Liao, G. Yin, Z. Huang, ACS Appl. Mater. Interfaces **8**, 24525–24535 (2016)
67. R. Dhilip Kumar, Y. Andou, S. Karuppuchamy, J Mater Sci. doi:[10.1007/s10854-016-6203-9](https://doi.org/10.1007/s10854-016-6203-9)